
MOTO: TOPOLOGY OPTIMIZATION FOR LARGE DEFORMATIONS VIA AN IMPLICIT MATERIAL POINT METHOD

Rahul Kumar Padhy
Department of Mechanical Engineering
University of Wisconsin-Madison
Madison, WI, USA
rkpadhy@wisc.edu

Aaditya Chandrasekhar
Department of Mechanical Engineering
Northwestern University
Evanston, IL, USA
aadityacs@northwestern.edu

Krishnan Suresh
Department of Mechanical Engineering
University of Wisconsin-Madison
Madison, WI, USA
ksuresh@wisc.edu

ABSTRACT

The Finite element method (FEM) has long served as the computational backbone for topology optimization (TO). However, for designing structures undergoing large deformations, conventional FEM-based TO often exhibits numerical instabilities due to severe mesh distortions, tangling, and large rotations, consequently leading to convergence failures.

To address this challenge, we present a TO framework based on the Material Point Method (MPM). MPM is a hybrid Lagrangian–Eulerian particle method, well-suited for simulating large deformations. In particular, we present an end-to-end differentiable implicit MPM framework for designing structures undergoing quasi-static hyperelastic large deformations. The effectiveness of the approach is demonstrated through validation studies encompassing both single and multi-material designs, including the design of compliant soft robotic grippers. The software accompanying this paper can be accessed at github.com/UW-ERSL/MOTO.

Keywords Material Point Method · Hyperelasticity · Topology Optimization · Differentiable Simulation

1 Introduction

Topology Optimization (TO) [1, 2] is a computational design method that optimizes material distribution within a design domain, subject to specified objectives and constraints. Structural TO has largely focused on small deformations with linear constitutive models [3, 4, 5]; for a comprehensive review, we refer the reader to [6, 7]. However, modern engineering increasingly demands designs that account for large deformations and nonlinear constitutive behaviors. Prominent applications include soft robotics [8], protective cellular structures [9, 10, 11], flexible electronics [12], and pneumatic actuators [13] (for example, see Figure 1).

Traditionally, the Finite Element Method (FEM) has been employed within TO to analyze structural responses (the forward problem) and compute sensitivities through adjoint methods (the backward problem). However, the Lagrangian mesh-based paradigm of FEM introduces significant challenges under large deformations. As elements deform with the material, they are prone to severe distortion [14], inversion, tangling [15, 16, 17], and fragmentation [18, 19], leading to numerical instability and convergence failure. The Material Point Method (MPM) [20] addresses these limitations by integrating Lagrangian and Eulerian descriptions. In MPM, the continuum is represented by moving Lagrangian material points carrying physical quantities (such as mass, stress, and velocity), while an Eulerian background grid facilitates the solution of the governing equations [21]. As illustrated in Figure 2(a), the initial body is discretized into a set of material points that reside within the computational domain. The relationship between these points, the domain, and the background grid is further clarified in the exploded view in Figure 2(b). Unlike traditional FEM, where

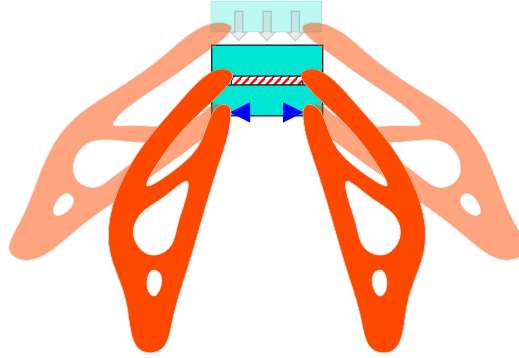


Figure 1: Design of soft robotic gripper undergoing large deformation.

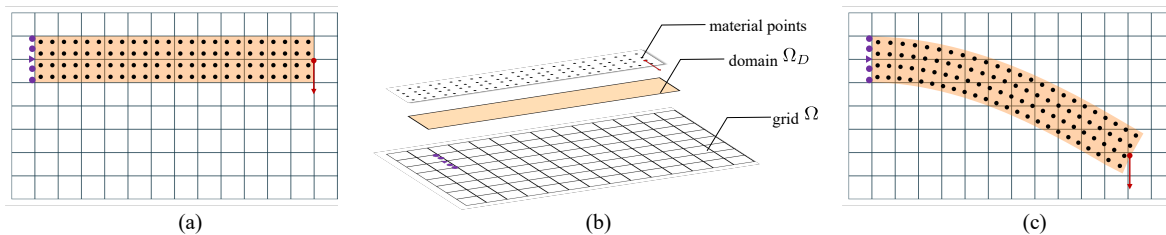


Figure 2: MPM discretization: (a) initial configuration, (b) exploded view showing material points, computational domain, and background grid, and (c) deformed configuration.

the mesh deforms with the material, the material points in MPM move through the fixed background grid as the body undergoes deformation (Figure 2(c)). This hybrid approach effectively mitigates mesh-related issues [22, 23].

For instance, consider the C-bracket example from [24] shown in Figure 3(a). In a standard FEM formulation (Figure 3(b)), the mesh deforms with the material, producing highly distorted and inverted elements that result in numerical instabilities. In contrast, the MPM formulation (Figure 3(c)) maintains a fixed background grid while material points track the deformed configuration, effectively bypassing mesh distortion regardless of deformation complexity. This renders MPM particularly advantageous for large-deformation TO.

While MPM has been predominantly tied to explicit time integration [25] and dynamic TO applications [26, 27], its application to quasi-static problems remains comparatively limited. Unlike explicit methods that utilize vector-based updates, quasi-static regimes necessitate implicit solvers. This requirement introduces significant numerical challenges,

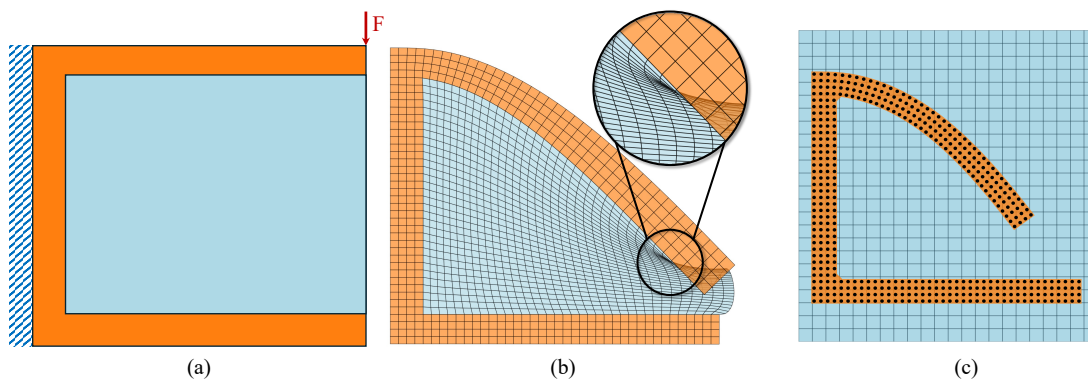


Figure 3: (a) C-bracket domain with boundary conditions. (b) Finite-element solution under the applied load, illustrating severe mesh distortion. (c) Material point method representation of the same problem, where material points move on a fixed background grid.

as it involves the assembly and inversion of a global tangent stiffness matrix within the MPM framework. This process is further complicated in quasi-static TO by the evolving particle-grid topology.

Various implicit MPM variants, such as the Generalized Interpolation Material Point (GIMP) [28, 21], the Dual Domain Material Point (DDMP) method, and the Convected Particle Domain Interpolation (CPDI) [29] have been proposed. Here we adopt and extend the GIMP method as it mitigates the grid-crossing instabilities inherent in standard MPM by providing C^1 continuity, which is critical for the stability and convergence of implicit solvers. While this formulation was recently applied to TO for small deformation linear elasticity [30], its extension to large deformation hyperelasticity remains unexplored.

To this end, we present MOTO, an implicit *m*aterial *p*oint framework for *t*opology *o*ptimization. The primary contributions of this work are as follows:

1. **Hyperelastic GIMP Formulation:** Implementation of a Hencky hyperelastic material model within the GIMP framework to capture the response of structures undergoing large deformations [21].
2. **Multimaterial Design Representation:** Integration of a neural network-based design representation [31] to enable spatially varying materials.
3. **End-to-End Differentiability:** Utilization of Automatic Differentiation (AD) [32] via the JAX library [33] to automate the complex sensitivity computations arising from neural representation, diverse objectives, constraints, and hyperelastic constitutive models.
4. **Application:** A demonstration of the framework’s capabilities through a case study on the design of compliant soft robotic grippers.

2 Related Work

This section reviews the state of the art in TO for structures undergoing large deformations across diverse applications. In addition, we review the numerical discretization methods used in large-deformation TO, spanning mesh-based and particle-based approaches.

Since the foundational work of [34], TO has matured into a powerful computational design tool used across a wide range of engineering applications [35, 2, 36, 37, 38]. Much of the classical structural TO literature has been developed under small-strain assumptions and linear constitutive models [3, 4, 5]. While suitable for structures undergoing small strains, these assumptions become restrictive when the structural response is governed by large deformations and nonlinear constitutive behaviors. This is the case in many contemporary applications, including soft robots undergoing large motions and hyperelastic deformation [39], cardiovascular stents undergoing large deployment deformations [40, 41], crashworthy structures dissipating energy through collapse [9, 10, 11], and architected metamaterials whose response depends on finite-strain mechanisms [42, 43, 44, 45].

Among the most active application areas of large-deformation TO are mechanical metamaterials, where the objective is often to tailor nonlinear effective response [42]. [43] demonstrated topology-optimized architectures with programmable Poisson’s ratios for large deformation. Building on this direction, [44] coupled density-based TO with nonlinear homogenization to design finite-strain auxetic metamaterials. More recently, [46] used multimaterial TO to obtain composite metastructures with programmable force–displacement responses. Another important application area of large deformation TO is biomedical design, where performance often depends on large deployment, expansion, or compliant motion under physiological loading. [40] designed a bi-stable cardiovascular stent whose deployment relies on snap-through between contracted and expanded stable configurations.

An important class of large-deformation TO problems involves contact, where the contact interface is generally unknown a priori and evolves together with the topology. [47] developed a framework for TO of multiple deformable bodies in contact using large-deformation mechanics. [48] extended the third-medium contact method to finite-strain TO with self-contact, introducing a regularization of the void region that makes the method suitable for very large deformations. Another practical application of large deformation TO is soft grippers, as they rely on material compliance to interact safely with delicate objects and adapt to diverse geometries [8, 49]. TO of a cable-driven soft gripper with geometric nonlinearity was presented in [50]. Furthermore, a framework for pressure-driven soft robots using nonlinear TO was proposed in [51]. Simultaneous shape and topology optimization of inflatable soft robots using finite-deformation hyperelasticity was formulated in [39]. Finally, large-deformation TO has also become important in crashworthiness [9], impact mitigation [10, 11], and elastoplastic design [52], where performance depends on irreversible deformation and energy dissipation. [53] extended elastoplastic TO to finite strains using rate-independent isotropic hardening plasticity and a multiplicative split of the deformation gradient. More recently, [52] presented a multimaterial finite-strain

elastoplastic formulation that simultaneously optimizes structural layout and material distribution, thereby expanding the design space for energy-dissipating and forming-dominated applications.

Underlying these diverse applications is a common computational challenge, namely the development of numerical discretization methods that can robustly handle large deformations during TO. Historically, most TO frameworks have relied on Lagrangian finite element discretizations [3], which provide accurate structural analysis in the small-deformation, linear-elastic regime and support density-based [54], level-set [55], and phase-field based TO formulations [56]. Extensions to large deformations have commonly been pursued through updated Lagrangian finite element formulations [57]. However, in density-based TO under large deformation, low-density regions can undergo severe mesh distortion, which may lead to element inversion and ill-conditioned stiffness matrices [58, 14]. Several stabilization strategies have therefore been proposed within nonlinear FEM, including element removal and reintroduction schemes [59, 60], energy-interpolation approaches for finite-strain fictitious-domain formulations [24], and additive hyperelastic regularization of distortion-prone elements [61]. Alternative discretizations have also been explored. Meshfree methods such as the element-free Galerkin method and reproducing kernel particle methods remove persistent mesh connectivity [62, 63] and have been applied in TO [64, 65]. However, they introduce additional complexity in enforcing boundary conditions and maintaining accuracy [66, 67].

Particle-based methods offer an alternative route for handling large motion and evolving geometry. In particular, the Material Point Method (MPM) combines Lagrangian material points with an Eulerian background grid and is well suited to large deformation and contact [20, 68]. Beyond its established use in geomechanics [69] and impact simulations [70], MPM has recently been integrated with TO [30], where the authors developed a quasi-static MPM-based TO framework in the small-deformation, linear-elastic regime, including analytical sensitivities and a study of cell-crossing effects. For dynamic problems, MPM-based TO has been used for trajectory-dependent objectives in which inertia is intrinsic to the formulation [26, 71]. In contrast, many design problems are governed by sequences of quasi-static equilibrium states, e.g., controlled actuation or sustained loading while maintaining stability [72, 73, 74]. For such applications, *MPM-based TO for quasi-static problems involving large deformation remains comparatively underexplored, motivating the present work.*

3 Proposed Method

This work introduces a topology optimization (TO) framework based on the Generalized Interpolation Material Point (GIMP) method [21], which is tailored for structures undergoing large deformations. We begin by prescribing a grid Ω , within which the design domain Ω_D is populated with material points as illustrated in Figure 2(b). The grid Ω is chosen sufficiently large to accommodate all expected deformed configurations of the body throughout the analysis. We assume that Dirichlet boundary conditions are applied to the grid nodes, while external loads are applied directly to the material points. We also assume the material constants for the assumed constitutive model (Hencky hyperelastic [21] in this work) have been prescribed. The primary objective is to determine the optimal material distribution that maximizes performance subject to design constraints.

The remainder of the methodology to achieve this objective is organized as follows: the governing equations are detailed in Section 3.2. The TO formulation is presented in Section 3.4. Sensitivity analysis via automatic differentiation is discussed in Section 3.5, and the complete optimization algorithm is summarized in Section 3.6.

For the sake of completeness, we begin by reviewing the material point method in Section 3.1. For a detailed treatment, we refer the readers to [21].

3.1 Overview of Material Point Method

We detail the numerical procedure of the Material Point Method (MPM) in this section. MPM combines Lagrangian and Eulerian descriptions to analyze structures undergoing large deformations. In this hybrid formulation, the continuum body is discretized into a set of Lagrangian material points (MPs) that are associated with the physical state variables, including mass, volume, deformation gradient, and stress. The governing force balance equations are solved on a fixed Eulerian grid. For instance, consider Figure 4 which details the core MPM steps as follows:

1. **Initialization:** The design domain Ω_D is populated with n_p material points, each assigned a uniform initial volume V_p^0 , mass $m_p = \rho V_p^0$, and identity deformation gradient. These points reside within a computational domain Ω composed of n_n grid nodes as illustrated in Figure 4(a). Furthermore, the Dirichlet boundary conditions are imposed on the grid nodes, while the loads are applied to the material points.
2. **Material point influence:** Each material point p interacts with the set of grid nodes whose GIMP basis functions have nonzero support over its influence domain, defined by lengths l^p , as shown in Figure 4(b).

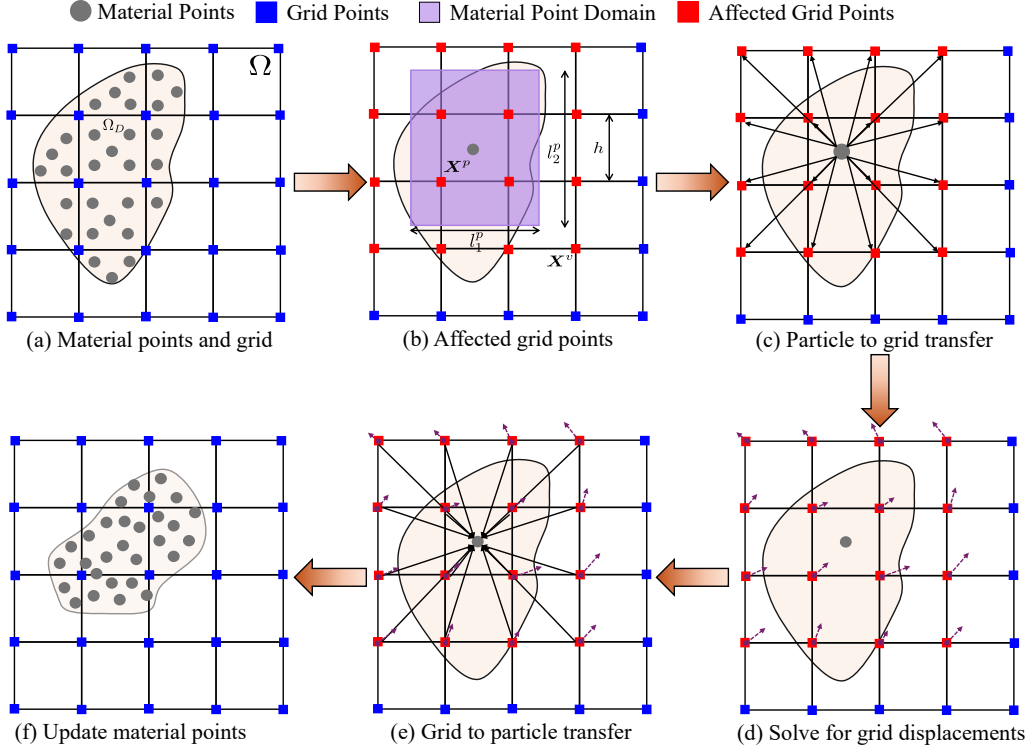


Figure 4: Illustration of the GIMP-based particle-grid coupling and update procedure. Material points are shown as gray circles, grid points as blue squares, and the domain of a representative material point as the shaded region. Grid points with nonzero GIMP support for that material point are highlighted in red. Panels (a)–(f) summarize the main MPM steps: initialization, identification of affected grid points, particle-to-grid transfer, solution of the force balance equations, grid-to-particle transfer, and update of the material points.

The mapping between the material points and the grid nodes is governed by the product-form GIMP shape functions $S^{vp} = \prod_i S_i^{vp}$, where the one-dimensional factors are defined in Equation (1).

$$S_i^{vp} = \begin{cases} \frac{(h + \frac{l_i^p}{2} + X_i^p - X_i^v)^2}{2h l_i^p}, & -h - \frac{l_i^p}{2} < X_i^p - X_i^v \leq -h + \frac{l_i^p}{2}, \quad [\text{A}] \\ 1 + \frac{X_i^p - X_i^v}{h}, & -h + \frac{l_i^p}{2} < X_i^p - X_i^v \leq -\frac{l_i^p}{2}, \quad [\text{B}] \\ 1 - \frac{(X_i^p - X_i^v)^2 + (\frac{l_i^p}{2})^2}{h l_i^p}, & -\frac{l_i^p}{2} < X_i^p - X_i^v \leq \frac{l_i^p}{2}, \quad [\text{C}] \\ 1 - \frac{X_i^p - X_i^v}{h}, & \frac{l_i^p}{2} < X_i^p - X_i^v \leq h - \frac{l_i^p}{2}, \quad [\text{D}] \\ \frac{(h + \frac{l_i^p}{2} - X_i^p + X_i^v)^2}{2h l_i^p}, & h - \frac{l_i^p}{2} < X_i^p - X_i^v \leq h + \frac{l_i^p}{2}. \quad [\text{E}] \end{cases} \quad (1)$$

Here h denotes the grid cell size, X_i^p is the material point coordinate, and X_i^v is the node coordinate along dimension i . The spatial gradient $\nabla_x S^{vp}$ is obtained analytically from the above by differentiating with respect to the current configuration coordinates [21].

The one-dimensional basis functions are illustrated in Figure 5, where the horizontal axis denotes the relative position of the material point $\delta = X_i^p - X_i^v$. The regions [A]–[E] shown in the figure correspond directly to the five cases in Equation (1). In regions [B] and [D], the generalized interpolation basis functions coincide with the conventional finite-element basis functions as the material point domain lies within a single grid cell.

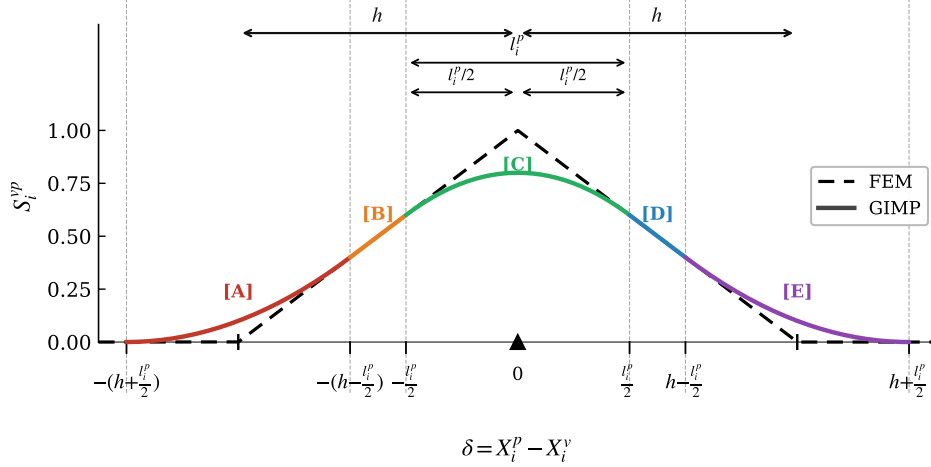


Figure 5: One-dimensional GIMP basis function S_i^{vp} versus the relative coordinate $\delta = X_i^p - X_i^v$, compared with the conventional finite-element basis function. Regions [A]–[E] correspond to the five cases in Equation (1).

In regions [A], [C], and [E], by contrast, the material point domain spans multiple background grid cells, and the basis functions therefore differ from the conventional finite-element form.

3. **Particle to grid transfer:** Once the grid nodes influenced by each material point have been identified, the force contributions are mapped from the material points to the grid as illustrated in Figure 4(c). Specifically, the external nodal force is assembled from body forces and prescribed particle loads using S^{vp} , whereas the internal nodal force is assembled from the particle stress state using the shape-function gradients, as described in Section 3.2.
4. **Solve on the grid:** With the nodal force vectors determined and the boundary conditions imposed, we solve the force balance equations on the grid to obtain the nodal displacement \mathbf{u}_v (see Figure 4(d)). As the problem is nonlinear, this force balance equations are solved iteratively using a Newton-Raphson procedure (see Section 3.2 for details).
5. **Grid to particle transfer:** After the grid solution is obtained, the nodal displacement field is interpolated back to the material points using the same GIMP shape functions S^{vp} , thereby yielding the displacement of each material point as illustrated in Figure 4(e).
6. **Update material points:** From the updated material point displacements, all physical state variables are updated: the deformation gradient, the Cauchy stress, the material point volume, GIMP domain half-lengths, and the material point positions as shown in Figure 4(f). Critically, the quantities stored on the grid are reset, whereas the updated state variables carried by the material points are retained. For highly nonlinear problems, the total applied load is divided into increments, and the above steps are repeated for each increment.

3.2 Governing Equations and Solution Procedure

Having described the numerical procedure of MPM, we now discuss the governing equations. In particular, to capture the structural response in the large deformation regime, we adopt a framework that accounts for geometric nonlinearity. Additionally, we employ a hyperelastic material model to describe the constitutive behavior.

Consider a design occupying a computational domain Ω as shown in Figure 2. The quasi-static response is governed by the force balance equation: Equation (2):

$$R(\mathbf{u}) := \nabla \cdot \boldsymbol{\sigma} + \rho \mathbf{b} = \mathbf{0} \quad , \text{ for } \mathbf{x} \in \Omega \quad (2)$$

where \mathbf{u} is the displacement field, $\boldsymbol{\sigma}$ is the Cauchy stress tensor, ρ is the material density, and \mathbf{b} is the specific body force. The prescribed displacement $\bar{\mathbf{u}}$ is applied on the grid nodes. Furthermore, point loads are applied on the material points at the prescribed locations. In the present work, traction boundary conditions are not considered. Their imposition in the MPM is nontrivial, as it generally requires an explicit representation of the physical boundary [75]. We therefore adopt a simplified treatment in which Dirichlet boundary conditions and point loads are considered.

We adopt an updated Lagrangian framework to describe the large deformation kinematics [21]. The deformation is characterized by the deformation gradient \mathbf{F} , defined as:

$$F_{ij} = \frac{\partial x_i}{\partial X_j} \quad (3)$$

where X_i and x_i denote the coordinates of material point p at the beginning of the load step and in the deformed configuration, respectively. For the constitutive response, we employ a Hencky hyperelastic model. The elastic logarithmic (Hencky) strain $\boldsymbol{\varepsilon}^e$ is defined as:

$$\boldsymbol{\varepsilon}^e = \frac{1}{2} \ln(\mathbf{B}), \quad \text{where } \mathbf{B} = \mathbf{F}\mathbf{F}^\top \quad (4)$$

is the left Cauchy- Green strain tensor and $\ln(\cdot)$ denotes the logarithm to base e . The Kirchhoff stress $\boldsymbol{\tau}$ is obtained using the isotropic linear elastic relation:

$$\boldsymbol{\tau} = \lambda \text{tr}(\boldsymbol{\varepsilon}^e) \mathbf{I} + 2\mu \boldsymbol{\varepsilon}^e. \quad (5)$$

where λ and μ are the Lamé parameters. Furthermore, for structures with small thickness relative to the in-plane dimensions, we enforce a plane-stress condition ($\sigma_{zz} = 0$), which yields:

$$\varepsilon_{zz}^e = -\frac{\lambda}{\lambda + 2\mu} (\varepsilon_{xx}^e + \varepsilon_{yy}^e) \quad (6)$$

Finally, the Cauchy stress is subsequently recovered via $\boldsymbol{\sigma} = \frac{1}{J} \boldsymbol{\tau}$, where $J = \det(\mathbf{F})$ [76].

Building upon the established MPM numerical procedure (Section 3.1), the discrete quasi-static force balance is enforced on the grid by assembling nodal internal and external force vectors. The internal force vector $\mathbf{f}_v^{\text{int}}$ is assembled from the particle stress contributions, which are defined as:

$$\mathbf{f}_{v,p}^{\text{int}} = V_p (\nabla_x S^{vp})^\top \boldsymbol{\sigma}_p, \quad (7)$$

where $\nabla_x S^{vp}$ denotes the spatial gradient of the GIMP shape function (Equation (1)), $\boldsymbol{\sigma}_p$ is the Cauchy stress at material point p , and V_p is the material point volume in the current configuration.

The external force vector $\mathbf{f}_v^{\text{ext}}$ is assembled from particle contributions due to body forces and applied point loads, which are defined as follows:

$$\mathbf{f}_{v,p}^{\text{ext}} = S^{vp} m_p \mathbf{b}_p + S^{vp} \mathbf{f}_p^{\text{ext}}, \quad (8)$$

where $m_p = \rho V_p$ is the material point mass, \mathbf{b}_p is the specific body force evaluated at material point p , and $\mathbf{f}_p^{\text{ext}}$ denotes externally applied point forces at material point p .

Combining Equation (7) and Equation (8), the discretized residual equation is:

$$\mathbf{R}(\mathbf{u}) = \mathbf{f}^{\text{int}}(\mathbf{u}) - \mathbf{f}^{\text{ext}} = \mathbf{0} \quad (9)$$

Here, \mathbf{f}^{int} and \mathbf{f}^{ext} denote the global nodal force vectors obtained by assembling the nodal contributions $\mathbf{f}_v^{\text{int}}$ $\mathbf{f}_v^{\text{ext}}$ for all grid nodes v .

Due to geometric and material nonlinearity, Equation (9) is solved using a Newton-Raphson scheme. At iteration k , the displacement correction $\delta \mathbf{u}^{(k)}$ is obtained from

$$\mathbf{K}^{(k)} \delta \mathbf{u}^{(k)} = -\mathbf{R}(\mathbf{u}^{(k)}), \quad (10)$$

The displacement is then updated $\mathbf{u}^{(k+1)} = \mathbf{u}^{(k)} + \delta \mathbf{u}^{(k)}$ until convergence. The global stiffness matrix \mathbf{K} is defined as:

$$\mathbf{K}^{(k)} = \left. \frac{\partial \mathbf{R}}{\partial \mathbf{u}} \right|_{\mathbf{u}^{(k)}} \quad (11)$$

Rather than deriving the tangent stiffness matrix analytically for the finite-strain kinematics and GIMP mapping, we compute it via automatic differentiation within JAX [33]. Furthermore, this end-to-end differentiability enables the sensitivity analysis required for TO, as discussed in Section 3.5.

3.3 Solver validation

Before detailing the optimization procedure, we validate the method’s accuracy and its implementation. We compare the accuracy of our implicit MPM solver against a classical benchmark: large-deformation bending of an elastic cantilever beam. This problem involves finite rotations and large strains comparable to those encountered in the TO examples. Furthermore, the problem has an analytical solution.

The benchmark consists of a cantilever beam of length $L = 10$ m and width $d_0 = 1$ m, as illustrated in Figure 6(a). Sliding boundary conditions are applied along the left edge, and the beam is fully fixed at its midpoint. A concentrated vertical force is applied at the midpoint of the right edge. The beam undergoes large deflections, with tip displacements approaching the beam length. The analytical solution for this problem was derived by [77].

For validation, the beam is modeled with the following material properties for the Hencky hyperelastic model: Young’s modulus $E = 12$ MPa and Poisson’s ratio $\nu = 0.2$. A total force of $f_0 = 100$ kN is applied incrementally over 50 equal load steps. The domain is discretized using the generalized interpolation material point method (GIMP) with 36 material points per background grid cell. Two mesh resolutions are tested: $h = 0.25$ m and $h = 0.125$ m.

Figure 6(b) shows the deformed configuration at the final load step for the $h = 0.125$ m discretization. The beam undergoes substantial bending, with the tip rotating nearly 90 degrees. The color contour displays the Cauchy stress component σ_{yy} , which exhibits the expected bending distribution: tension on the outer region and compression on the inner region.

Figure 6(c) compares the normalized force-displacement response against the analytical solution. Both horizontal (u^*/L) and vertical (v^*/L) tip displacements are plotted against the normalized applied force (f/f_{\max}). The MPM results for both mesh resolutions show excellent agreement with the analytical solution across the entire loading range. The difference between the two discretizations is negligible, indicating mesh convergence. At the maximum load, the vertical tip displacement reaches approximately $0.8L$, demonstrating the framework’s capability to handle large deformations accurately.

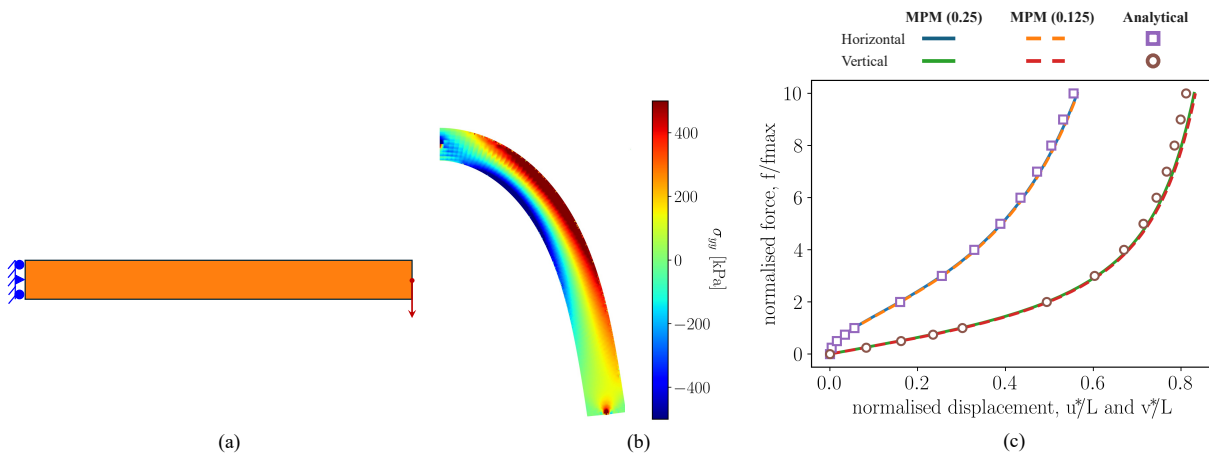


Figure 6: Validation of our implicit MPM framework for the large-deformation bending of a cantilever beam. (a) Beam geometry, boundary conditions, and loading. (b) Deformed configuration at the final load step for the $h = 0.125$ m discretization, colored by the Cauchy stress component σ_{yy} . (c) Normalized force-displacement response comparing MPM predictions for two mesh resolutions with the analytical solution of [77].

3.4 Topology Optimization

With the established and validated GIMP-based MPM framework, we now formulate the TO problem. The goal is to find the optimal material distribution within Ω_D the specified objective and constraints. In the present work, we consider both single- and multi-material TO. We begin with a single-material formulation based on particle-wise pseudodensity, which serves as the most direct extension of standard density-based TO to the MPM setting. We then introduce a more general multi-material formulation based on a coordinate-based neural network. The following sections detail the proposed methodology.

3.4.1 Single-Material Topology Optimization

For single-material TO, we adopt a particle-wise pseudodensity representation. This formulation is a natural extension of the standard element-wise density approach used in finite-element-based TO to the material point setting.

Specifically, we assign each material point p a pseudodensity $\gamma_p \in [0, 1]$, where $\gamma_p = 1$ denotes solid material and $\gamma_p = 0$ denotes void. Intermediate values are allowed during optimization to facilitate gradient-based optimization. Observe that in contrast to conventional FEM formulations, where the design variables are associated with grid elements, here the design variables are carried directly by the material points. Consequently, the material distribution is transported with the Lagrangian particles throughout the updated-Lagrangian MPM solve.

3.4.2 Multi-Material Topology Optimization

Many applications require more than a single material. For instance, soft robotic grippers must balance flexibility with structural rigidity, requiring design with spatially varying stiffness. While the particle-wise pseudodensity formulation could, in principle, be extended to multi-material TO, we instead adopt a coordinate-based neural-network representation. This representation subsumes the single-material case as a special case but is introduced here for multi-material design due to advantages discussed next.

Multi-material design requires specifying what material exists at each location. Towards this, let S denote the number of a priori prescribed materials. Then at each point \mathbf{x} we define volume fractions $\mathbf{v}(\mathbf{x}) = [v_1, \dots, v_S]$, where $\sum_{s=1}^S v_s(\mathbf{x}) = 1$ and $v_s(\mathbf{x}) \geq 0$; $\forall \mathbf{x}$.

Adopting [31], we parameterize this field using a neural network (NN) $\mathbf{v}(\mathbf{x}; \mathbf{w})$, where \mathbf{w} denotes the weights of the NN. The NN maps spatial coordinates from the design domain to the volume fractions Figure 7. This representation offers three key advantages over conventional approaches where design variables are explicitly tied to the simulation discretization (in this case, the material points):

- The network architecture inherently enforces the partition-of-unity constraint via its output activation.
- The design is decoupled from the background grid, allowing for a compact set of design variables independent of simulation resolution.
- The material field is analytically defined everywhere, facilitating the recovery of crisp, high-resolution topologies.

The proposed network architecture, as illustrated in Figure 7 consists of the following components:

1. **Input Layer:** The spatial coordinates $\mathbf{x} \in \mathbb{R}^d$ ($d = 2$ dimensions) are propagated through the network as input.
2. **Fourier Projection:** The Euclidean coordinates are mapped to a higher-dimensional feature space using a Fourier projection layer to mitigate the spectral bias of standard multi-layer perceptrons and enable the representation of high-frequency topological features [78]. This projection promotes faster convergence and allows the network to capture intricate structural details that would otherwise be smoothed out.
3. **Hidden Layers:** The feature vector is propagated through a series of dense hidden layers (two layers with 40 neurons each) using ReLU activation functions [79].
4. **Output Layer:** The final layer consists of S neurons corresponding to the volume fractions of the S materials. A Softmax activation function is applied to the output, intrinsically satisfying $\sum_{s=1}^S v_s = 1$ and $0 \leq v_s \leq 1$.

The trainable weights and biases \mathbf{w} of this network constitute the primary design variables for the optimization process. Furthermore, the weights \mathbf{w} are initialized using Xavier normal initialization [80]. The network is initialized to produce a spatially uniform volume-fraction field across all phases.

3.4.3 Material Model

Having described the design representation, we now detail the interpolation of the material properties. In particular, we use the standard Solid Isotropic Material with Penalization (SIMP) [81] scheme for the Lamé parameters. Given the Lamé parameters $\lambda_1, \dots, \lambda_S, \mu_1, \dots, \mu_S$ of the S available materials, the effective Lamé parameters λ_p, μ_p can be obtained as:

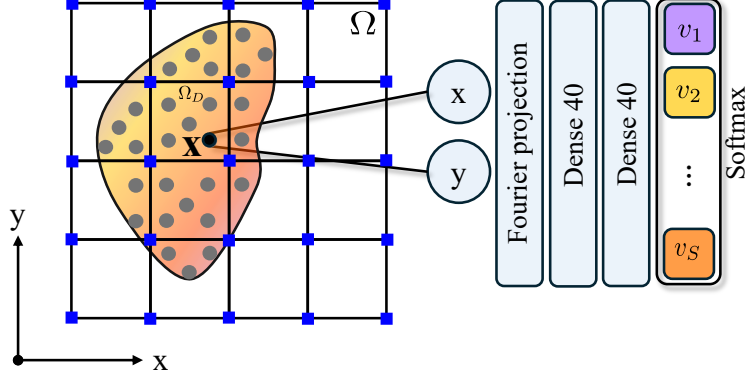


Figure 7: Coordinate-based neural network used for multi-material TO. The network maps spatial coordinates in the design domain to material volume fractions.

$$\lambda_p = \sum_{s=1}^S (v_{s,p})^q \lambda_s, \quad \mu_p = \sum_{s=1}^S (v_{s,p})^q \mu_s \quad (12)$$

Furthermore, we employ standard continuation schemes [82] for the penalty parameter q . For a single-material design, Equation (12) reduces to:

$$\lambda_p = \gamma_p^q \lambda_0, \quad \mu_p = \gamma_p^q \mu_0 \quad (13)$$

Furthermore, the mass density is interpolated linearly for multi-material formulation as:

$$\rho_p = \sum_{s=1}^S v_{s,p} \rho_s \quad (14)$$

For single-material formulation, this reduces to $\rho_p = \gamma_p \rho$.

3.4.4 Design Objective

Having obtained the interpolated material properties, we now discuss the design objective. We consider two formulations in our examples, namely, the minimization of compliance and the design of compliant mechanisms.

Compliance: We consider the design of load-bearing structures by minimizing the structural compliance:

$$J_c = \mathbf{f}^{\text{ext}\top} \mathbf{u}^* \quad (15)$$

where \mathbf{f}^{ext} is the external force and \mathbf{u}^* is the converged material point displacement.

Compliant Mechanisms: We also consider the design of compliant soft robotic grippers. Here, the goal is to maximize motion transmission from input to output. In other words, an input actuation, such as a pneumatic pressure, must produce a desired gripping motion at the output port. Concurrently, the mechanism must maintain sufficient rigidity to grasp objects without excessive internal deformation. We quantify this trade-off through the ratio of mutual strain energy (MSE) to the sum of input (SE_{in}) and output (SE_{out}) strain energies [83]:

$$J_m = -\frac{\text{MSE}}{SE_{\text{in}} + SE_{\text{out}}} = -\frac{\mathbf{f}_{\text{in}}^{\text{ext}\top} \mathbf{v}^*}{\mathbf{f}_{\text{in}}^{\text{ext}\top} \mathbf{u}^* + \mathbf{f}_{\text{out}}^{\text{ext}\top} \mathbf{v}^*} \quad (16)$$

Here \mathbf{u}^* is the displacement field under the actual input load $\mathbf{f}_{\text{in}}^{\text{ext}}$, and \mathbf{v}^* is the displacement field under a pseudo load $\mathbf{f}_{\text{out}}^{\text{ext}}$ applied at the output port in the desired actuation direction.

3.4.5 Constraints

To ensure cost-effective designs, we impose constraints on the amount of material used.

Volume Constraint: For single-material design, we impose the standard volume constraint as:

$$g_v \equiv \frac{1}{V^*} \sum_{p=1}^{n_p} V_p^0 \gamma_p - 1 \leq 0 \quad (17)$$

where V_p^0 is the reference volume of particle p and V^* is the prescribed volume limit.

Mass Constraint: For multi-material design, we enforce a mass constraint:

$$g_m \equiv \frac{1}{M^*} \sum_{p=1}^{n_p} V_p^0 \rho_p(\mathbf{v}_p) - 1 \leq 0 \quad (18)$$

where ρ_p is the interpolated density from Equation (14) and M^* is the allowable mass.

3.5 Sensitivity Analysis

A critical step in gradient-based TO is the computation of sensitivities, the derivatives of objectives and constraints with respect to design variables. The sensitivity analysis for this work is particularly complex because it must account for nonlinear hyperelasticity with large-strain kinematics and a computational pipeline that integrates the MPM solver with a coordinate-based neural network.

To address this complexity, we construct an end-to-end differentiable pipeline using the automatic differentiation (AD) capabilities of the JAX framework. This allows us to avoid the laborious and error-prone process of manually deriving sensitivity expressions. By implementing the entire forward analysis within JAX, from the neural design mapping to the nonlinear MPM solver, the framework computes the required derivatives to machine precision using reverse-mode AD.

We emphasize three challenges inherent to our structural simulation. The first arises from the use of iterative schemes, such as the Newton-Raphson method, to solve the nonlinear governing equations at each load step. A naive application of AD would unroll derivative computation across every solver iteration, computing the total derivative via the chain rule:

$$\frac{d\mathbf{u}^{(K)}}{d\gamma} = \frac{\partial\mathbf{u}^{(K)}}{\partial\mathbf{u}^{(K-1)}} \cdot \frac{\partial\mathbf{u}^{(K-1)}}{\partial\mathbf{u}^{(K-2)}} \cdot \dots \cdot \frac{\partial\mathbf{u}^{(1)}}{\partial\mathbf{u}^{(0)}} \cdot \frac{\partial\mathbf{u}^{(0)}}{\partial\gamma} \quad (19)$$

This approach is computationally expensive and memory-intensive, as both scale with the number of iterations K . To overcome this inefficiency, we apply the Implicit Function Theorem (IFT) [84]. Given that the residual vanishes at convergence, $\mathbf{R}(\gamma, \mathbf{u}^{(K)}) = \mathbf{0}$, and the tangent stiffness $\mathbf{K} = \partial\mathbf{R}/\partial\mathbf{u}$ is invertible, the derivative follows directly:

$$\frac{d\mathbf{u}^{(K)}}{d\gamma} = -\mathbf{K}^{-1} \frac{\partial\mathbf{R}}{\partial\gamma} \quad (20)$$

This enables direct computation of derivatives from the final converged solution, bypassing the need to backpropagate through the iterative solution history.

The second challenge stems from the incremental nature of the simulation, which creates a significant memory bottleneck for the adjoint sensitivity method. Computing gradients for history-dependent objectives requires access to the structural state from all previous load steps, and storing this entire configuration history is often infeasible for long loading sequences. We mitigate this issue by employing a checkpointing scheme [85, 86]. This technique stores the system's state at select increments, and during the backward pass, intermediate configurations are recomputed on the fly. This method reduces memory requirements at the cost of a moderate increase in computation time, making the optimization of large-scale nonlinear problems feasible.

The third challenge arises from differentiating through the hyperelastic constitutive model. The Hencky strain (Equation (4)) requires the matrix logarithm of \mathbf{B} . Let the eigendecomposition be:

$$\mathbf{B} = \mathbf{Q} \text{diag}(\boldsymbol{\Lambda}) \mathbf{Q}^\top \quad (21)$$

where \mathbf{Q} contains the eigenvectors as columns and $\boldsymbol{\Lambda} = [\Lambda_1, \dots, \Lambda_d]^\top$ collects the eigenvalues. The matrix logarithm follows by spectral mapping:

$$\ln(\mathbf{B}) = \mathbf{Q} \text{diag}(\ln \boldsymbol{\Lambda}) \mathbf{Q}^\top \quad (22)$$

Differentiating this operation requires the Fréchet derivative of the matrix logarithm. Using the Daleckiĭ–Kreĭn formula [87], the directional derivative in direction \mathbf{E} is:

$$d \ln(\mathbf{B})[\mathbf{E}] = \mathbf{Q} (\mathbf{L} \odot (\mathbf{Q}^\top \mathbf{E} \mathbf{Q})) \mathbf{Q}^\top \quad (23)$$

where \odot denotes the Hadamard (elementwise) product and \mathbf{L} is the Loewner matrix with entries:

$$L_{ij} = \begin{cases} \frac{\ln \Lambda_i - \ln \Lambda_j}{\Lambda_i - \Lambda_j}, & i \neq j \\ \frac{1}{\Lambda_i}, & i = j \end{cases} \quad (24)$$

The off-diagonal terms become ill-conditioned when $\Lambda_i \approx \Lambda_j$. Under large rotations with minimal stretch, the eigenvalues of \mathbf{B} cluster near unity, triggering this singularity. We regularize by switching to the diagonal form $L_{ij} = 1/\Lambda_i$ when $|\Lambda_i - \Lambda_j| < \epsilon$, ($\epsilon = 10^{-12}$ in our experiments), which corresponds to the limiting value as $\Lambda_j \rightarrow \Lambda_i$.

3.6 Algorithm

We summarize the optimization framework, which integrates the differentiable MPM solver with a gradient-based optimizer, below.

1. **Discretization:** The computational domain Ω is discretized into a fixed Eulerian grid and the design domain Ω_D into a set of Lagrangian material points. The grid provides the computational mesh for the force balance equation solve. The material points serve as quadrature points for stress integration and store the design field.
2. **Initialization:** Each particle is assigned an initial volume V_p^0 , mass $m_p = \rho V_p^0$, and identity deformation gradient. For single-material design, the pseudo-densities initialize uniformly as $\gamma_p = V^*$. Additionally, for multi-material design, the network weights \mathbf{w} are initialized via Xavier normal initialization, producing uniform volume fractions $v_s = 1/S$.
3. **Boundary Conditions:** Dirichlet conditions prescribe nodal displacements on Γ_d . Point loads are applied through $\mathbf{f}_p^{\text{ext}}$ on material points.
4. **Optimization Loop:** Each iteration is detailed as follows:
 - (a) **Design-to-physics mapping:** For pseudo-density, compute λ_p and μ_p via Equation (13). For neural network, evaluate $\mathbf{v}(\mathbf{x}_p; \mathbf{w})$ and compute properties via Equations (12) and (14).
 - (b) **Forward solve.** At each load step, solve $\mathbf{R} = \mathbf{0}$ via Newton-Raphson until $\|\mathbf{R}\| < \epsilon_{\text{NR}}$. Update particle states: positions \mathbf{x}_p , deformation gradients, stresses $\boldsymbol{\sigma}_p$, and volumes V_p .
 - (c) **Objective and constraint evaluation:** Compute J_c or J_m and g_v or g_m from the converged configuration.
 - (d) **Sensitivity analysis:** Reverse-mode AD propagates gradients from objectives to design variables. IFT bypasses Newton iteration unrolling. Checkpointing manages memory across load steps.
 - (e) **Design update:** For pseudo-density, update γ_p via Method of Moving Asymptotes (MMA) [88] or optimality criteria. For neural network, update weights \mathbf{w} via ADAM [89].
 - (f) **Continuation scheme:** Increase the SIMP exponent q toward its target value.
 - (g) **Convergence check:** Terminate if $|(\Delta J_m/J_m) \text{ or } (\Delta J_c/J_c)| < \epsilon_{\text{opt}}$ or the maximum iteration count is reached.

4 Numerical Experiments

This section presents numerical experiments demonstrating the proposed framework. All simulations are performed on an Apple MacBook M4 Pro using the JAX library [33]. Unless otherwise specified, the default parameters are as follows:

- **Mesh:** The computational domain is discretized using a structured background grid. The domain sizes (Ω and Ω_D) and resolution vary by example and are specified in each subsection.
- **Material points:** We assign four material points per element per spatial dimension, yielding a total of 16 material points per element in the two-dimensional setting.
- **Neural network:** For NN-based optimization problems, the topology is parameterized via a network with a 100-term Fourier projection layer and two hidden layers of 40 neurons each, using a softmax output activation.

- **SIMP continuation:** The penalization exponent q is initialized to 1 and incremented by 5×10^{-2} per iteration to a maximum of 5.
- **Newton-Raphson solver:** For the Newton-Raphson solver, we use a convergence tolerance $\epsilon_{NR} = 10^{-7}$, a maximum of 50 iterations, and a backtracking line search (Armijo parameter $c = 10^{-4}$) [90, 91].
- **Optimizer:** For single-material problems, we employ the Method of Moving Asymptotes (MMA) [88] with a move limit of 10^{-2} . For multi-material problems, we use the ADAM [89] optimizer with a learning rate of 10^{-2} .
- **Constraint handling:** For single-material problems, constraints are enforced directly within MMA. For multi-material neural network problems, we formulate the constrained optimization problem using a log-barrier penalty ([92]) with an initial parameter $\tau_0 = 3$ and growth factor $\mu = 1.02$ is used.
- **Convergence:** The optimization terminates when relative objective change $|(\Delta J_m/J_m)$ or $(\Delta J_c/J_c)| < 10^{-4}$ or after a maximum number of iterations specified per example.

Table 1: Material properties for single-material examples.

Parameter	Value
Lame's lambda λ_0	4.3×10^9
Lame's mu μ_0	1.1×10^9
Mass density ρ	1600 kg/m^3
Thickness t	1.0 mm

4.1 Validation

We first validate the proposed framework on a TO of a cantilever beam. The setup of the problem is illustrated in Figure 8. Here, we consider a grid (Ω) with 80×40 cells. Furthermore, we consider a rectangular design domain (Ω_D) of dimensions 0.12×0.03 m that occupies 54×27 grid cells. Additionally, a Dirichlet condition where the left edge is clamped is imposed on the grid cells while a downward force f is applied at a material point on the mid-right edge of the design domain. The volume fraction constraint is set to 0.5 (corresponds to an allowed mass of 2.88×10^{-3} kg) of the total domain volume Ω_D .

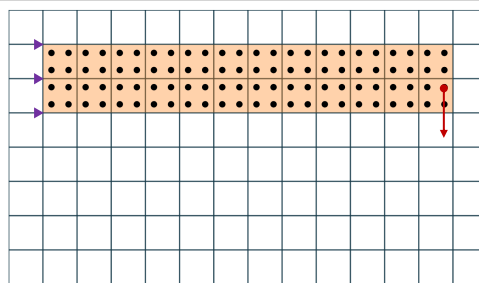


Figure 8: Representative domain discretization showing the boundary conditions, grid, and material points for a mid-cantilever beam.

Figure 9 shows the optimized topologies for increasing load magnitudes: $f = 0.1, 0.25,$ and 0.5 kN. Under the smallest load, the topology is nearly symmetric about the horizontal midplane (Figure 9(a)). This resembles the solution obtained from linear modeling. As the load increases, the optimized designs become increasingly asymmetric (Figure 9(b–c)). A single tensile member emerges on the right-hand side of the beam. This member grows in both length and width with increasing load. The emergence of this tensile member reflects the dominant role of geometric nonlinearity at large deflections. After significant deformation, the tensile member provides the most direct load transmission path. As the nonlinear effect intensifies, this member becomes the primary load-bearing component. The final optimized topologies are consistent with solutions reported in existing studies [24].

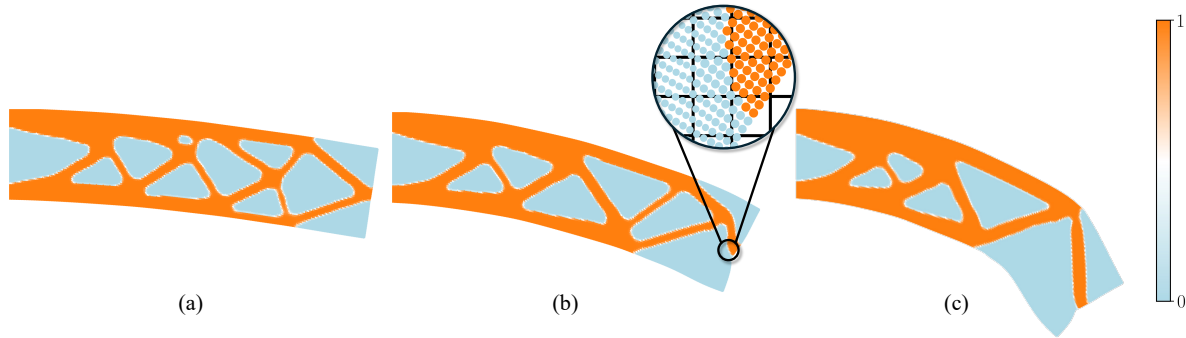


Figure 9: Optimized designs and corresponding deformed configurations for increasing loads: (a) ($f = 0.1$ kN, $J_c = 1.3$), (b) ($f = 0.25$ kN, $J_c = 7.6$), and (c) ($f = 0.5$ kN, $J_c = 24.9$).

Figure 10 shows the convergence history for the $f = 0.25$ kN case. Both the objective (compliance) and the constraint (volume fraction) exhibit stable convergence. The optimization was completed in 4 minutes and 36 seconds. Similar convergence behavior was observed for the other experiments.

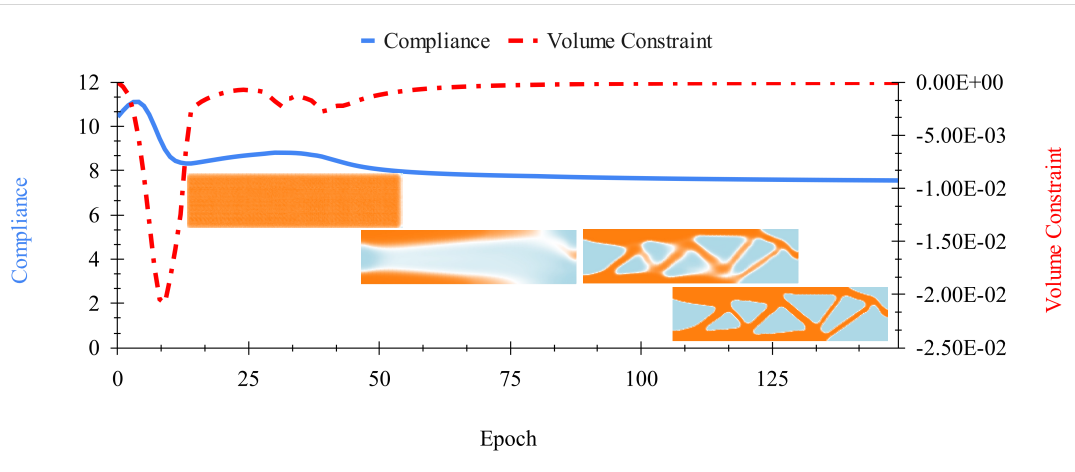


Figure 10: Convergence of the objective and constraints for a prescribed load of 0.25 kN.

4.2 Compliance Minimization of Multimaterial Designs

We now extend the cantilever benchmark to multiple materials. The problem setup remains unchanged. Three materials (plus void) with distinct Lamé parameters and mass density, as shown in (Table 2) are used. A mass constraint of $M^* = 2.88 \times 10^{-3}$ kg is imposed.

Table 2: Material properties for multi-material examples.

Material	Color	λ (GPa)	μ (GPa)	ρ (kg/m ³)
1	Violet	17.1	4.3	4000
2	Yellow	4.3	1.1	1600
3	Orange	1.4	0.35	750
4	White (Void)	1.4×10^{-4}	3.5×10^{-5}	10^{-1}

Figure 11 shows the optimized multi-material designs for each load case. Compared with the corresponding single-material designs, the multi-material formulation achieves lower compliance for the same allowable mass due to the additional design freedom provided by multiple materials. Furthermore, Figure 12 shows the convergence history for the $f = 0.25$ kN case. Both the objective (compliance) and constraint (mass constraint) exhibit stable convergence.

The optimization completed in 5 minutes and 12 seconds. Similar convergence behavior was observed for the other experiments.

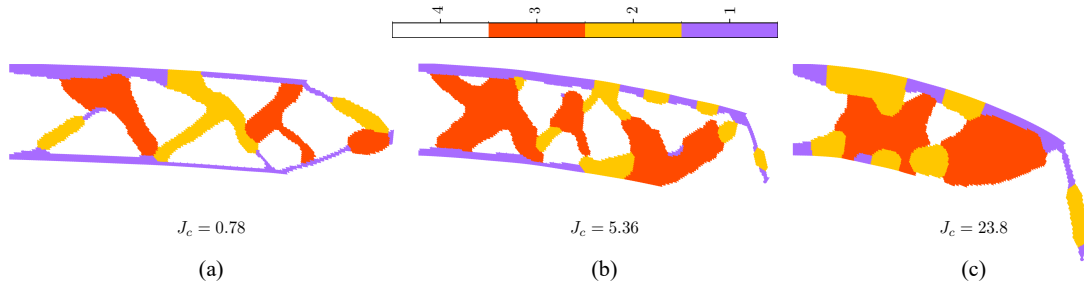


Figure 11: Optimized design obtained from TO using multiple materials for increasing loads: (a) ($f = 0.1$ kN, $J_c = 0.78$), (b) ($f = 0.25$ kN, $J_c = 5.36$), and (c) ($f = 0.5$ kN, $J_c = 23.8$).

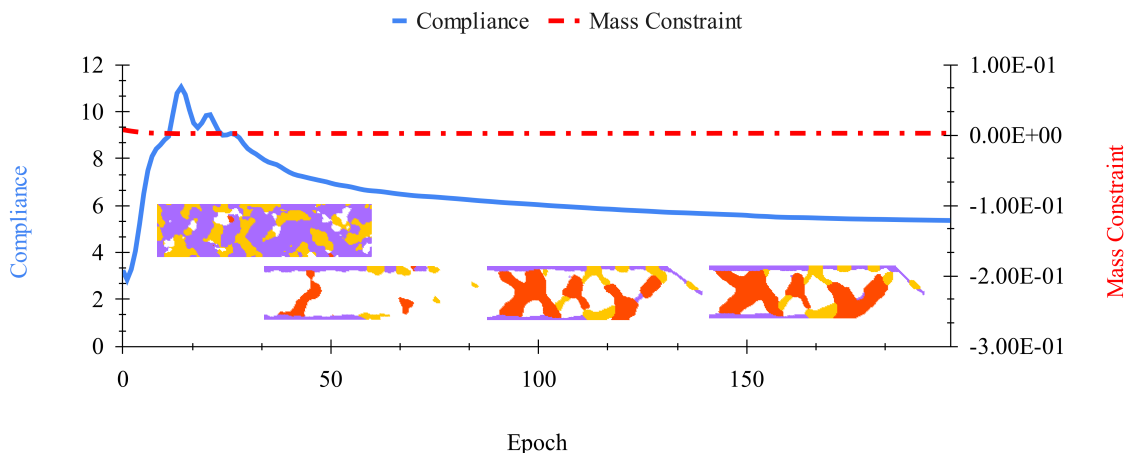


Figure 12: Convergence of the objective and constraints of multi-material TO for a prescribed load of 0.25 kN.

4.3 Design of Grippers

The design of soft robotic grippers requires both flexibility for grasping and stiffness for load-bearing. We demonstrate the proposed framework on the design of compliant grippers [93], using the material properties listed in Table 2.

Figure 13(a) shows the design domain and boundary conditions. The domain is a trapezoid with a horizontal extent of 160 mm and a height of 70 mm. A solid non-design region of dimensions 90×1.75 mm spans the bottom edge; this region represents the contact surface that interacts with grasped objects. The top-right corner receives an input force f_{in} , while a fixed support constrains the bottom edge near the output port. The objective is to maximize the output displacement f_{out} at the left corner of the contact surface for a prescribed input.

Figure 13(b) shows the optimized topology and Figure 13(c) shows the assembled configuration under the applied load.

5 Conclusion

In this work, we present MOTO, a material point method (MPM)-based topology optimization (TO) framework for the design of structures undergoing quasi-static large deformations. In particular, we utilize the implicit Generalized Interpolation Material Point (GIMP) variant of MPM to resolve mesh distortion issues inherent to conventional Lagrangian finite element methods. We incorporated a Hencky hyperelastic constitutive model to capture the response of structures in the finite-strain regime. Furthermore, we leveraged an end-to-end differentiable pipeline implemented

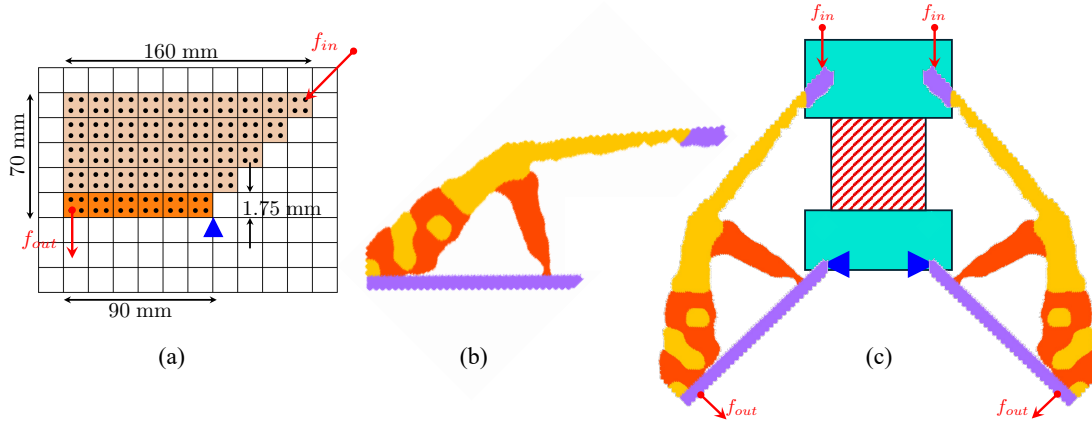


Figure 13: Design of compliant grippers. (a) Representative design domain, non-design contact region, boundary conditions, and input/output ports for a single gripper. (b) Optimized gripper topology obtained using the proposed framework. (c) Assembled gripper configuration under the applied input forces f_{in} .

in JAX to automate the computation of sensitivities. We presented an optimization framework that supports both single-material pseudodensity and multi-material coordinate neural network design representations. The effectiveness of the framework was demonstrated through validation studies and the design of compliant mechanisms, specifically a soft robotic gripper.

The present study offers several avenues for future research. First, the current formulation focused exclusively on hyperelastic materials. However, many engineering applications involve structures that undergo large plastic deformation, such as energy-absorbing devices. The extension of the framework to include elastoplasticity is of significant interest. Second, while we considered compliance and the design of compliant mechanisms, incorporating stress constraints within the large-deformation MPM context will be essential to prevent material failure. Third, future work should focus on extending soft robotic systems to involve coupled design and actuation and optimizing for dynamic trajectories. Fourth, extending the framework to 3D configurations is necessary for practical applicability. This will require leveraging efficient GPU-accelerated implementations such as [94] to address computational demands. Fifth, given that MPM naturally handles contact, extending the framework to design contact structures such as [95] presents an interesting avenue. Sixth, investigating the imposition of manufacturing constraints within the context of material point-based design representations is a necessary future step. Seventh, MPM's hybrid Lagrangian-Eulerian formulation is well suited to problems involving large topological changes, including crack initiation and propagation, dynamic fracture [96, 97], and impact-driven fragmentation [68], making it a promising direction for future TO research. Finally, it is of interest to validate optimized designs experimentally by fabricating and testing soft robotic prototypes.

Compliance with ethical standards

The authors declare that they have no conflict of interest.

Replication of Results

The Python source code is available in a public GitHub repository at github.com/UW-ERSL/MOTO. This implementation is also provided as supplementary material to the version published in the journal.

References

- [1] Martin Philip Bendsoe and Ole Sigmund. *Topology optimization: theory, methods, and applications*. Springer Science & Business Media, 2013.
- [2] Ole Sigmund and Kurt Maute. Topology optimization approaches: A comparative review. *Structural and multidisciplinary optimization*, 48(6):1031–1055, 2013.

- [3] Ole Sigmund. A 99 line topology optimization code written in matlab. *Structural and multidisciplinary optimization*, 21(2):120–127, 2001.
- [4] Jikai Liu, Andrew T Gaynor, Shikui Chen, Zhan Kang, Krishnan Suresh, Akihiro Takezawa, Lei Li, Junji Kato, Jinyuan Tang, Charlie CL Wang, et al. Current and future trends in topology optimization for additive manufacturing. *Structural and multidisciplinary optimization*, 57(6):2457–2483, 2018.
- [5] Chao Wang, Zhi Zhao, Ming Zhou, Ole Sigmund, and Xiaojia Shelly Zhang. A comprehensive review of educational articles on structural and multidisciplinary optimization. *Structural and Multidisciplinary Optimization*, 64(5):2827–2880, 2021.
- [6] Joshua D Deaton and Ramana V Grandhi. A survey of structural and multidisciplinary continuum topology optimization: post 2000. *Structural and multidisciplinary optimization*, 49(1):1–38, 2014.
- [7] Fabian Wein, Peter D Dunning, and Julián A Norato. A review on feature-mapping methods for structural optimization. *Structural and multidisciplinary optimization*, 62(4):1597–1638, 2020.
- [8] George B Crowley, Xianpai Zeng, and Hai-Jun Su. A 3d printed soft robotic gripper with a variable stiffness enabled by a novel positive pressure layer jamming technology. *IEEE Robotics and Automation Letters*, 7(2):5477–5482, 2022.
- [9] Jiao Jia, Daicong Da, Jianxing Hu, and Sha Yin. Crashworthiness design of periodic cellular structures using topology optimization. *Composite Structures*, 271:114164, 2021.
- [10] Hao Deng, Lin Cheng, Xuan Liang, Devlin Hayduke, and Albert C To. Topology optimization for energy dissipation design of lattice structures through snap-through behavior. *Computer Methods in Applied Mechanics and Engineering*, 358:112641, 2020.
- [11] Oliver Giraldo-Londoño, Rogelio A Muñetón-López, Paul L Barclay, Xiatian Zhuang, Duan Z Zhang, and Zhen Chen. Toward engineering lattice structures with the material point method (mpm). *Engineering with Computers*, pages 1–19, 2025.
- [12] Yunfeng Luo, Shiyuan Qu, Shutian Liu, and YongAn Huang. Nonlinear electromechanical topology optimization method for stretchable electronic interconnect structures. *Engineering with Computers*, 41(1):117–133, 2025.
- [13] Hiroki Kobayashi, Farzad Gholami, S Macrae Montgomery, Masato Tanaka, Liang Yue, Changyoung Yuhn, Yuki Sato, Atsushi Kawamoto, H Jerry Qi, and Tsuyoshi Nomura. Computational synthesis of locomotive soft robots by topology optimization. *Science Advances*, 10(30):eadn6129, 2024.
- [14] Nam-Sua Lee and Klaus-Jurgen Bathe. Effects of element distortions on the performance of isoparametric elements. *International Journal for numerical Methods in engineering*, 36(20):3553–3576, 1993.
- [15] Bhagyashree Prabhune and Krishnan Suresh. A computationally efficient isoparametric tangled finite element method for handling inverted quadrilateral and hexahedral elements. *Computer Methods in Applied Mechanics and Engineering*, 405:115897, 2023.
- [16] Bhagyashree Prabhune and Krishnan Suresh. An isoparametric tangled finite element method for handling higher-order elements with negative jacobian. *Computational Mechanics*, 73(1):159–176, 2024.
- [17] Josh Danczyk and Krishnan Suresh. Finite element analysis over tangled simplicial meshes: Theory and implementation. *Finite Elements in Analysis and Design*, 70:57–67, 2013.
- [18] M Cervera, M Chiumenti, and R Codina. Mesh objective modeling of cracks using continuous linear strain and displacement interpolations. *International Journal for Numerical Methods in Engineering*, 87(10):962–987, 2011.
- [19] L Mishnaevsky Jr, N Lippmann, and S Schmauder. Computational modeling of crack propagation in real microstructures of steels and virtual testing of artificially designed materials. *International journal of fracture*, 120(4):581–600, 2003.
- [20] Deborah Sulsky, Zhen Chen, and Howard L Schreyer. A particle method for history-dependent materials. *Computer methods in applied mechanics and engineering*, 118(1-2):179–196, 1994.
- [21] William M Coombs and Charles E Augarde. Ample: a material point learning environment. *Advances in Engineering Software*, 139:102748, 2020.
- [22] YP Lian, X Zhang, and Y Liu. Coupling of finite element method with material point method by local multi-mesh contact method. *Computer Methods in Applied Mechanics and Engineering*, 200(47-48):3482–3494, 2011.
- [23] Zdzisław Więckowski. The material point method in large strain engineering problems. *Computer methods in applied mechanics and engineering*, 193(39-41):4417–4438, 2004.

- [24] Fengwen Wang, Boyan Stefanov Lazarov, Ole Sigmund, and Jakob Søndergaard Jensen. Interpolation scheme for fictitious domain techniques and topology optimization of finite strain elastic problems. *Computer Methods in Applied Mechanics and Engineering*, 276:453–472, 2014.
- [25] Yuanming Hu, Yu Fang, Ziheng Ge, Ziyin Qu, Yixin Zhu, Andre Pradhana, and Chenfanfu Jiang. A moving least squares material point method with displacement discontinuity and two-way rigid body coupling. *ACM Transactions on Graphics (TOG)*, 37(4):1–14, 2018.
- [26] Changyoung Yuhn, Yuki Sato, Hiroki Kobayashi, Atsushi Kawamoto, and Tsuyoshi Nomura. 4d topology optimization: Integrated optimization of the structure and self-actuation of soft bodies for dynamic motions. *Computer Methods in Applied Mechanics and Engineering*, 414:116187, 2023.
- [27] Yuki Sato, Hiroki Kobayashi, Changyoung Yuhn, Atsushi Kawamoto, Tsuyoshi Nomura, and Noboru Kikuchi. Topology optimization of locomoting soft bodies using material point method. *arXiv preprint arXiv:2203.16793*, 2022.
- [28] TJ Charlton, WM Coombs, and CE Augarde. igimp: An implicit generalised interpolation material point method for large deformations. *Computers & Structures*, 190:108–125, 2017.
- [29] Alireza Sadeghirad, Rebecca M Brannon, and Jeff Burghardt. A convected particle domain interpolation technique to extend applicability of the material point method for problems involving massive deformations. *International Journal for numerical methods in Engineering*, 86(12):1435–1456, 2011.
- [30] Sanghyeon Park, Byeonghyeon Goh, and Hayoung Chung. Topology optimization with material point method: investigation into the design sensitivity and the effect of shape functions. *Engineering with Computers*, pages 1–18, 2025.
- [31] Aaditya Chandrasekhar and Krishnan Suresh. Multi-material topology optimization using neural networks. *Computer-Aided Design*, 136:103017, 2021.
- [32] Rahul Kumar Padhy, Krishnan Suresh, and Aaditya Chandrasekhar. Toflux: A differentiable topology optimization framework for multiphysics fluidic problems. *arXiv preprint arXiv:2508.17564*, 2025.
- [33] James Bradbury, Roy Frostig, Peter Hawkins, Matthew James Johnson, Chris Leary, Dougal Maclaurin, George Necoara, Adam Paszke, Jake VanderPlas, Skye Wanderman-Milne, and Qiao Zhang. JAX: composable transformations of Python+NumPy programs, 2018.
- [34] Martin Philip Bendsøe and Noboru Kikuchi. Generating optimal topologies in structural design using a homogenization method. *Computer methods in applied mechanics and engineering*, 71(2):197–224, 1988.
- [35] Joe Alexandersen and Casper Schousboe Andreassen. A review of topology optimisation for fluid-based problems. *Fluids*, 5(1):29, 2020.
- [36] Rahul Kumar Padhy and Aaditya Chandrasekhar. Photos: topology optimization of photonic components using a shape library. *Engineering with Computers*, 41(2):1141–1153, 2025.
- [37] Rahul Kumar Padhy, Krishnan Suresh, and Aaditya Chandrasekhar. Tomatoes: Topology and material optimization for latent heat thermal energy storage devices. *Applied Energy*, 406:127322, 2026.
- [38] Rahul Kumar Padhy, Aaditya Chandrasekhar, and Krishnan Suresh. Fluto: Graded multi-scale topology optimization of large contact area fluid-flow devices using neural networks. *Engineering with Computers*, 40(2):971–987, 2024.
- [39] Anna Dalklint, Mathias Wallin, and Daniel Tortorelli. Simultaneous shape and topology optimization of inflatable soft robots. *Computer Methods in Applied Mechanics and Engineering*, 420:116751, 2024.
- [40] Kai A James and Haim Waisman. Layout design of a bi-stable cardiovascular stent using topology optimization. *Computer Methods in Applied Mechanics and Engineering*, 305:869–890, 2016.
- [41] Huipeng Xue, Zhen Luo, Terry Brown, and Susann Beier. Design of self-expanding auxetic stents using topology optimization. *Frontiers in bioengineering and biotechnology*, 8:736, 2020.
- [42] Fengwen Wang, Ole Sigmund, and Jakob Søndergaard Jensen. Design of materials with prescribed nonlinear properties. *Journal of the Mechanics and Physics of Solids*, 69:156–174, 2014.
- [43] Anders Clausen, Fengwen Wang, Jakob Søndergaard Jensen, Ole Sigmund, and Jennifer A Lewis. Topology optimized architectures with programmable poisson’s ratio over large deformations. *Advanced Materials*, 27(37):5523–5527, 2015.
- [44] Guodong Zhang and Kapil Khandelwal. Computational design of finite strain auxetic metamaterials via topology optimization and nonlinear homogenization. *Computer Methods in Applied Mechanics and Engineering*, 356:490–527, 2019.

- [45] Anna Dalklint, Filip Sjövall, Mathias Wallin, Seth Watts, and Daniel Tortorelli. Computational design of metamaterials with self contact. *Computer Methods in Applied Mechanics and Engineering*, 417:116424, 2023.
- [46] Weichen Li, Fengwen Wang, Ole Sigmund, and Xiaojia Shelly Zhang. Design of composite structures with programmable elastic responses under finite deformations. *Journal of the Mechanics and Physics of Solids*, 151:104356, 2021.
- [47] Felipe Fernandez, Michael A Puso, Jerome Solberg, and Daniel A Tortorelli. Topology optimization of multiple deformable bodies in contact with large deformations. *Computer Methods in Applied Mechanics and Engineering*, 371:113288, 2020.
- [48] Gore Lukas Bluhm, Ole Sigmund, and Konstantinos Poullos. Internal contact modeling for finite strain topology optimization. *Computational Mechanics*, 67(4):1099–1114, 2021.
- [49] Daniela Rus and Michael T Tolley. Design, fabrication and control of soft robots. *Nature*, 521(7553):467–475, 2015.
- [50] Rixin Wang, Xianmin Zhang, Benliang Zhu, Hongchuan Zhang, Bicheng Chen, and Haonan Wang. Topology optimization of a cable-driven soft robotic gripper. *Structural and Multidisciplinary Optimization*, 62(5):2749–2763, 2020.
- [51] Brandon Caasenbrood, Alexander Pogromsky, and Henk Nijmeijer. A computational design framework for pressure-driven soft robots through nonlinear topology optimization. In *2020 3rd IEEE international conference on soft robotics (RoboSoft)*, pages 633–638. IEEE, 2020.
- [52] Yingqi Jia and Xiaojia Shelly Zhang. Multimaterial topology optimization for finite strain elastoplasticity: theory, methods, and applications. *Computer Methods in Applied Mechanics and Engineering*, 449:118445, 2026.
- [53] Mathias Wallin, Viktor Jönsson, and Eric Wingren. Topology optimization based on finite strain plasticity. *Structural and multidisciplinary optimization*, 54(4):783–793, 2016.
- [54] Erik Andreassen, Anders Clausen, Mattias Schevenels, Boyan S Lazarov, and Ole Sigmund. Efficient topology optimization in matlab using 88 lines of code. *Structural and Multidisciplinary Optimization*, 43(1):1–16, 2011.
- [55] Grégoire Allaire, François Jouve, and Anca-Maria Toader. Structural optimization using sensitivity analysis and a level-set method. *Journal of computational physics*, 194(1):363–393, 2004.
- [56] Akihiro Takezawa, Shinji Nishiwaki, and Mitsuru Kitamura. Shape and topology optimization based on the phase field method and sensitivity analysis. *Journal of Computational Physics*, 229(7):2697–2718, 2010.
- [57] Thomas Buhl, Claus BW Pedersen, and Ole Sigmund. Stiffness design of geometrically nonlinear structures using topology optimization. *Structural and Multidisciplinary Optimization*, 19(2):93–104, 2000.
- [58] Ricardo Doll Lahuerta, Eduardo T Simões, Eduardo MB Campello, Paulo M Pimenta, and Emilio CN Silva. Towards the stabilization of the low density elements in topology optimization with large deformation. *Computational Mechanics*, 52(4):779–797, 2013.
- [59] Tyler E Bruns and Daniel A Tortorelli. An element removal and reintroduction strategy for the topology optimization of structures and compliant mechanisms. *International journal for numerical methods in engineering*, 57(10):1413–1430, 2003.
- [60] Gil Ho Yoon and Yoon Young Kim. Element connectivity parameterization for topology optimization of geometrically nonlinear structures. *International journal of solids and structures*, 42(7):1983–2009, 2005.
- [61] Yangjun Luo, Michael Yu Wang, and Zhan Kang. Topology optimization of geometrically nonlinear structures based on an additive hyperelasticity technique. *Computer methods in applied mechanics and engineering*, 286:422–441, 2015.
- [62] Ted Belytschko, Yun Yun Lu, and Lei Gu. Element-free galerkin methods. *International journal for numerical methods in engineering*, 37(2):229–256, 1994.
- [63] Andreas Neofytou, Renato Picelli, Tsung-Hui Huang, Jiun-Shyan Chen, and H Alicia Kim. Level set topology optimization for design-dependent pressure loads using the reproducing kernel particle method. *Structural and Multidisciplinary Optimization*, 61(5):1805–1820, 2020.
- [64] Vahid Shobeiri. The topology optimization design for cracked structures. *Engineering Analysis with Boundary Elements*, 58:26–38, 2015.
- [65] Juan Zheng, Xujing Yang, and Shuyao Long. Topology optimization with geometrically non-linear based on the element free galerkin method. *International Journal of Mechanics and Materials in Design*, 11(3):231–241, 2015.
- [66] Sahil Garg and Mohit Pant. Meshfree methods: a comprehensive review of applications. *International Journal of Computational Methods*, 15(04):1830001, 2018.

- [67] Yury Krongauz and Ted Belytschko. Enforcement of essential boundary conditions in meshless approximations using finite elements. *Computer Methods in Applied Mechanics and Engineering*, 131(1-2):133–145, 1996.
- [68] Alban De Vaucorbeil, Vinh Phu Nguyen, Sina Sinaie, and Jian Ying Wu. Material point method after 25 years: Theory, implementation, and applications. *Advances in applied mechanics*, 53:185–398, 2020.
- [69] Kenichi Soga, E Alonso, Alba Yerro, K Kumar, and Samila Bandara. Trends in large-deformation analysis of landslide mass movements with particular emphasis on the material point method. *Géotechnique*, 66(3):248–273, 2016.
- [70] Peng Huang, X Zhang, S Ma, and X Huang. Contact algorithms for the material point method in impact and penetration simulation. *International journal for numerical methods in engineering*, 85(4):498–517, 2011.
- [71] Yuki Sato, Hiroki Kobayashi, Changyoung Yuhn, Atsushi Kawamoto, Tsuyoshi Nomura, and Noboru Kikuchi. Topology optimization of locomoting soft bodies using material point method: Y. sato et al. *Structural and Multidisciplinary Optimization*, 66(3):50, 2023.
- [72] Ali Shiva, SM Hadi Sadati, Yohan Noh, Jan Fraś, Ahmad Ataka, Helge Würdemann, Helmut Hauser, Ian D Walker, Thrishantha Nanayakkara, and Kaspar Althoefer. Elasticity versus hyperelasticity considerations in quasistatic modeling of a soft finger-like robotic appendage for real-time position and force estimation. *Soft Robotics*, 6(2):228–249, 2019.
- [73] Yitong Zhou, Leon M Headings, and Marcelo J Dapino. Modeling of soft robotic grippers integrated with fluidic prestressed composite actuators. *Journal of Mechanisms and Robotics*, 14(3):031001, 2022.
- [74] Kanghyeon Lee and Youngsu Cha. Quasi-static analysis of an electrohydraulic actuator for a soft gripper. *Sensors and Actuators A: Physical*, 352:114214, 2023.
- [75] Y Bing, M Cortis, TJ Charlton, WM Coombs, and CE Augarde. B-spline based boundary conditions in the material point method. *Computers & Structures*, 212:257–274, 2019.
- [76] Eduardo A de Souza Neto, Djordje Peric, and David RJ Owen. *Computational methods for plasticity: theory and applications*. John Wiley & Sons, 2008.
- [77] Terry Kim Molstad. *Finite deformation analysis using the finite element method*. PhD thesis, University of British Columbia, 1977.
- [78] Matthew Tancik, Pratul Srinivasan, Ben Mildenhall, Sara Fridovich-Keil, Nithin Raghavan, Utkarsh Singhal, Ravi Ramamoorthi, Jonathan Barron, and Ren Ng. Fourier features let networks learn high frequency functions in low dimensional domains. *Advances in neural information processing systems*, 33:7537–7547, 2020.
- [79] Abien Fred Agarap. Deep learning using rectified linear units (relu). *arXiv preprint arXiv:1803.08375*, 2018.
- [80] Xavier Glorot and Yoshua Bengio. Understanding the difficulty of training deep feedforward neural networks. In *Proceedings of the thirteenth international conference on artificial intelligence and statistics*, pages 249–256. JMLR Workshop and Conference Proceedings, 2010.
- [81] Martin P Bendsøe and Ole Sigmund. Material interpolation schemes in topology optimization. *Archive of applied mechanics*, 69(9):635–654, 1999.
- [82] Ole Sigmund and Joakim Petersson. Numerical instabilities in topology optimization: a survey on procedures dealing with checkerboards, mesh-dependencies and local minima. *Structural optimization*, 16(1):68–75, 1998.
- [83] Benliang Zhu, Xianmin Zhang, Hongchuan Zhang, Junwen Liang, Haoyan Zang, Hai Li, and Rixin Wang. Design of compliant mechanisms using continuum topology optimization: A review. *Mechanism and Machine Theory*, 143:103622, 2020.
- [84] Mathieu Blondel, Quentin Berthet, Marco Cuturi, Roy Frostig, Stephan Hoyer, Felipe Llinares-López, Fabian Pedregosa, and Jean-Philippe Vert. Efficient and modular implicit differentiation. *Advances in neural information processing systems*, 35:5230–5242, 2022.
- [85] Qiqi Wang, Parviz Moin, and Gianluca Iaccarino. Minimal repetition dynamic checkpointing algorithm for unsteady adjoint calculation. *SIAM Journal on Scientific Computing*, 31(4):2549–2567, 2009.
- [86] Kai A James and Haim Waisman. Topology optimization of viscoelastic structures using a time-dependent adjoint method. *Computer Methods in Applied Mechanics and Engineering*, 285:166–187, 2015.
- [87] Nicholas J Higham. *Functions of matrices: theory and computation*. SIAM, 2008.
- [88] Krister Svanberg. The method of moving asymptotes—a new method for structural optimization. *International journal for numerical methods in engineering*, 24(2):359–373, 1987.
- [89] Diederik P Kingma and Jimmy Ba. Adam: A method for stochastic optimization. *arXiv preprint arXiv:1412.6980*, 2014.

- [90] Larry Armijo. Minimization of functions having lipschitz continuous first partial derivatives. *Pacific Journal of mathematics*, 16(1):1–3, 1966.
- [91] Jorge Nocedal. Numerical optimization, 2006.
- [92] Hoel Kervadec, Jose Dolz, Jing Yuan, Christian Desrosiers, Eric Granger, and Ismail Ben Ayed. Constrained Deep Networks: Lagrangian Optimization via Log-Barrier Extensions. 4 2019.
- [93] Yunsong Du, Pengwei Zhang, and Tiemin Li. Topology optimization of compliant grippers based on stress constraints. *Journal of Mechanisms and Robotics*, 17(6):061001, 2025.
- [94] Yidong Zhao, Xuan Li, Chenfanfu Jiang, and Jinhyun Choo. Geowarp: An automatically differentiable and gpu-accelerated implicit mpm framework for geomechanics based on nvidia warp. *Advances in Engineering Software*, 212:104072, 2026.
- [95] Andreas H Frederiksen, Anna Dalklint, Ole Sigmund, and Konstantinos Poullos. Improved third medium formulation for 3d topology optimization with contact. *Computer Methods in Applied Mechanics and Engineering*, 436:117595, 2025.
- [96] John A Nairn. Material point method calculations with explicit cracks. *Computer Modeling in Engineering and Sciences*, 4(6):649–664, 2003.
- [97] Emmanouil G Kakouris and Savvas P Triantafyllou. Phase-field material point method for brittle fracture. *International Journal for Numerical Methods in Engineering*, 112(12):1750–1776, 2017.